Journal of Alloys and Compounds xxx (xxxx) xxx

Contents lists available at ScienceDirect

Journal of Alloys and Compounds

journal homepage: http://www.elsevier.com/locate/jalcom

Vibrational modes and quantum zero-point energy of hydrogen in $ZrH_{0.0155}$ and ZrH_2

Timothy R. Prisk [a, *], Alexander I. Kolesnikov [b], Garrett E. Granroth [b], Jun-Li Lin [c], Brent J. Heuser [c]

[a] Center for Neutron Research, National Institute of Standards and Technology, Gaithersburg, MD, 20899-6100, United States
[b] Neutron Scattering Division, Oak Ridge National Laboratory, Oak Ridge, TN, 37831, United States
[c] Department of Nuclear, Plasma, and Radiological Engineering, University of Illinois, Urbana, IL, 61801, United States

ARTICLE INFO

Article history:
Received 31 May 2019
Received in revised form
7 October 2019
Accepted 27 October 2019
Available online xxx

Keywords:
Inelastic neutron scattering
Anharmonic lattice dynamics
Nuclear reactors
Hydrides
Transition-metal alloys

ABSTRACT

We report on an inelastic neutron scattering study of the proton dynamics in $ZrH_{0.0155}$ and ε-ZrH_2. In particular, we present measurements of the incoherent dynamic structure factor, generalized vibrational density of states, and proton momentum distribution of these two materials. Our results are generally consistent with theoretical predictions of Elsässer et al. [Mat. Res. Soc. Symp. Proc. **453** 221−226 (1997)]. They argued that the effective Born-Oppenheimer potential experienced by the hydrogen atoms in ε-ZrH_2 is nearly isotropic and harmonic at energies below 0.3 eV, but becomes anisotropic and anharmonic for higher energies. At low temperatures, the proton momentum distribution is dominated by the quantum-mechanical ground state of the protons. We find that it assumes a Gaussian shape, consistent with the concept that the potential surface is approximately harmonic for small displacements of the hydrogen atoms. However, the anharmonicity of the potential becomes readily apparent in the excited states of the hydrogen atoms, as the harmonic approximation breaks down in the description of the multiphonon bands.

Published by Elsevier B.V.

1. Introduction

Zirconium-based alloys are used throughout the world as fuel cladding and channel boxes in light water nuclear reactors (LWRs). These alloys perform especially well in the primary coolant of LWRs, despite undergoing uniform corrosion, hydrogen pickup, radiation damage and embrittlement, and the evolution of significant tensile hoop stress due to fuel swelling and fission gas release [1]. All of these processes are understood and the world-wide nuclear industry continues to make important advancements of Zr-based alloys [2].

The behavior of hydrogen is especially important since the solubility limit is exceeded, leading to hydride formation in the cladding [3]. This has a few important consequences. First, hydride formation causes embrittlement. Second, the hydrogen can be released during off-normal temperature transients. Third, it is possible for the hydrides to re-orient during long-term storage, leading to delayed hydride cracking [4] that can result in radionuclide release. However, the likelihood of off-normal transients and clad failure during storage is low. Experience indicates a failure rate on the order of 10^{-6}/year/rod during normal LWR operation [5].

The formation, structure, and properties of the zirconium hydrides are fully reviewed in Refs. [6–8]. At low concentrations, hydrogen occupies tetrahedral interstitial positions in the crystal lattice of α-phase (hcp, $P6_3/mmc$) and β-phase (bcc, Im-3m) zirconium. At higher concentrations, the zirconium structure transforms into the hydride phases: δ-$ZrH_{x>1.43}$ (fcc, Fm-3m) and ε-$ZrH_{1.745\leq x\leq 2}$ (bct, $I4/mmm$). In these phases, too, the hydrogen atoms occupy tetrahedral interstitial sites. Fig. 1 illustrates the crystal structures of the α, δ, and ε phases near room temperature.

Here, we are interested in more fundamental aspects of hydrogen in Zr that do not necessarily couple to LWR technology and the associated utility of these alloys in primary coolant. A fundamental scientific understanding of these materials depends upon an accurate determination of the effective potential acting on the hydrogen. Neutron scattering techniques are well-suited to addressing this problem as they offer direct probes of the local structure and dynamics of materials containing hydrogen [9,10].

* Corresponding author.
E-mail address: tprisk@alumni.iu.edu (T.R. Prisk).

https://doi.org/10.1016/j.jallcom.2019.152832
0925-8388/Published by Elsevier B.V.

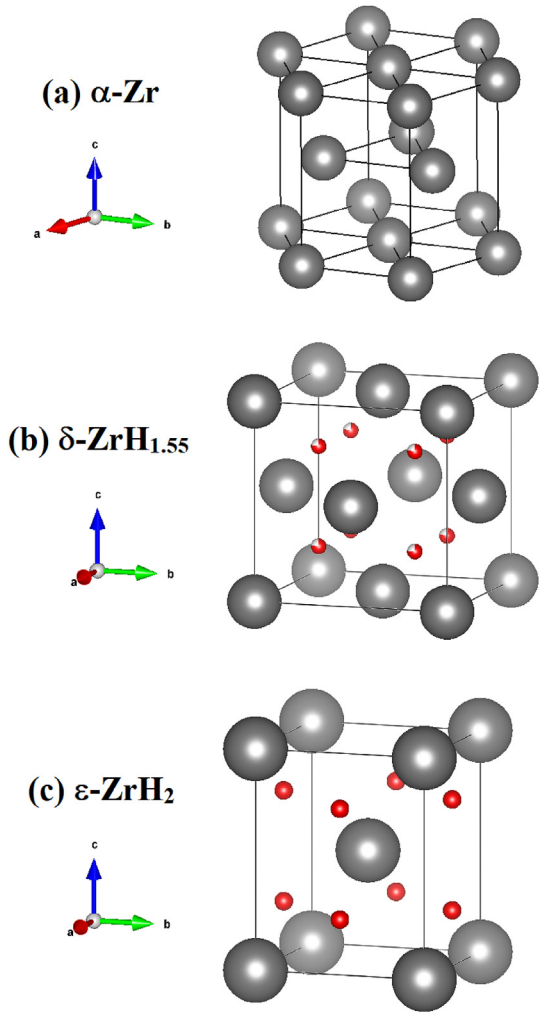

Fig. 1. The crystal structure of (a) α-Zr [58] (space group: hcp $P6_3/mmc$; primitive unit cell dimensions: $a = b = 3.24205(3)$ Å, $c = 5.16643(9)$ Å, $\alpha = \beta = 90°$, $\gamma = 120°$, $V = 47.03$ Å^3); (b) δ-$ZrH_{1.55}$ [59] (space group: fcc Fm-3m; unit cell dimensions: $a = b = c = 4.776(3)$, $\alpha = \beta = \gamma = 90°$, $V = 108.94$ Å^3); and (c) ε-ZrH_2 [59] (space group: bct $I4/mmm$; unit cell dimensions: $a = b = 3.518(3)$ Å, $c = 4.47(3)$ Å, $\alpha = \beta = \gamma = 90°$, $V = 55.03$ Å^3). Zr atoms are shown as dark gray spheres while H atoms are shown as red spheres. The wedge on the H atoms in panel (b) signifies a partial occupancy of the tetrahedral interstitial sites of 77.5%.

A carefully studied case is ε-ZrH_2. Ikeda et al. examined the local potential and hydrogen wavefunctions of ZrH_2 by means of inelastic neutron scattering (INS) [11–13]. They found that the vibrational motion of hydrogen within ZrH_2 can be described as an isotropic harmonic oscillator with a level spacing of $\hbar\omega = 147$ meV. Evans et al. have performed neutron Compton scattering measurements of the proton momentum distribution $n(k)$ of ZrH_2 at low temperatures [14,15]. They report that $n(k)$ is Gaussian and that the average proton kinetic energy $\langle E_K \rangle$ is 112±2 meV. This is consistent with the ground state wavefunction inferred by Ikeda et al.; the virial theorem requires $\langle E_K \rangle = \frac{3}{4}\hbar\omega$ at zero temperature. Elsässer et al. calculated the effective Born-Oppenheimer potential of hydrogen within ZrH_2 by means of density functional theory [16]. They find that the potential well is approximately isotropic and harmonic below 300 meV, but it becomes anisotropic and anharmonic at higher energies. It is noteworthy to compare the behavior of ε-ZrH_2 with uranium nitride, where it was recently shown that nitrogen acts as a simple harmonic oscillator in a uranium matrix over many energy levels [17,18].

In this paper, we present a comparative neutron scattering study of the hydrogen dynamics within $ZrH_{0.0155}$ and ZrH_2. The experiment was performed using the SEQUOIA spectrometer at Oak Ridge National Laboratory. In particular, we report high-precision measurements of the generalized vibrational density of states $G(E)$ and the average proton kinetic energy $\langle E_K \rangle$ as a function of temperature. We show the known hydrogen solubility for dissolution (the terminal solid solution solubility for dissolution, TSSD) and for precipitation (TSSP) in Fig. 2. Inelastic neutron scattering measurements were performed at 6 K, 550 K, and 617 K, the latter two being shown on the figure. In addition, we have recently measured the TSSD and TSSP for our sample at a hydrogen concentration of 170 μg/g [19]; these measurements are indicated in Fig. .2 as well. Thus, the data set presented here encompasses ε-ZrH_2 and α-Zr + δ-$ZrH_{1.6}$, where α-Zr is the H solid solution phase.

To date, nearly all neutron Compton scattering studies of proton momentum distributions have been carried out with indirect geometry instruments based upon a resonance foil technique [20,21]. This is because, until recently, only these instruments have been capable of simultaneously achieving an appropriately wide kinematic range and sufficiently fine energy resolution [22]. The application of direct geometry instruments has been limited almost completely to quantum fluids and solids, such as ^{4}He [23–26], ^{3}He [27], para-H_2 [28], and Ne [29]. However, the advent of high flux spallation sources with fine resolution chopper spectrometers designed for operation in the eV energy range enable Compton scattering studies of protons in condensed matter on direct geometry instruments. This paper demonstrates the effectiveness of SEQUOIA [30,31] at the Spallation Neutron Source [32] for such studies.

The paper is organized as follows. In Section 2, we briefly review the conceptual basis our experiment in the neutron scattering formalism. Section 3 provides the details of the sample characterization, experimental setup, and data treatment. In Section 4, we present our experimental data and compare the observed INS spectra of $ZrH_{0.0155}$ and ZrH_2. We apply the Impulse Approximation in Section 5 to obtain empirical estimates of the average atomic kinetic energy $\langle E_K \rangle$. Our findings are summarized in the Conclusion. An appendix outlining our calculations of the inelastic energy resolution of SEQUOIA has also been included.

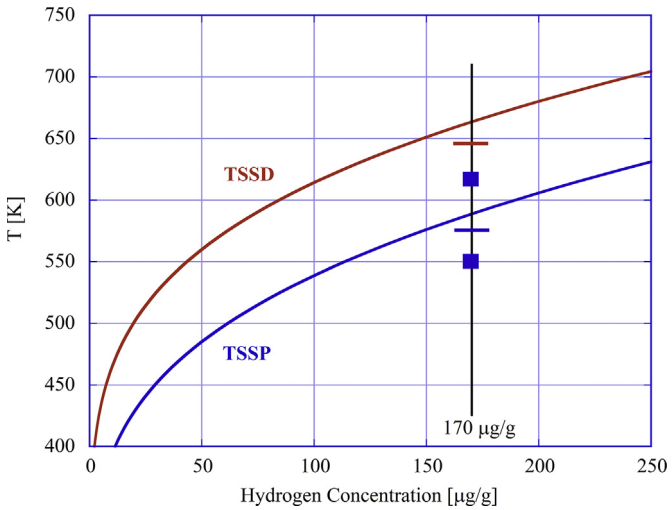

Fig. 2. The solid solution phase behavior of $ZrH_{0.0155}$ (170 μg/g). The dissolution (TSSD) and precipitation (TSSP) boundaries reported in Ref. [3] are shown as red and blue curves, respectively. The short solid lines indicate our previous determination of the boundaries at this concentration, discussed in Ref. [19]. Blue squares denote thermodynamic conditions considered in this paper.

Please cite this article as: T.R. Prisk et al., Vibrational modes and quantum zero-point energy of hydrogen in $ZrH_{0.0155}$ and ZrH_2, Journal of Alloys and Compounds, https://doi.org/10.1016/j.jallcom.2019.152832

2. Neutron scattering formalism

Inelastic neutron scattering techniques provide direct experimental probes of the atomic-scale dynamics of condensed matter systems [33,34]. In this paper, we will consider the powder-averaged dynamic structure factor $S(Q,E)$ of $ZrH_{0.0155}$ and ZrH_2. Two different regimes of momentum $\hbar Q$ and energy E transfer will be investigated. At "low" Q ($\lesssim$20 Å^{-1}), the scattering from these materials is dominated by acoustic and optical phonons as well as local modes. At "high" Q ($\gtrsim$20 Å^{-1}), the scattering is determined by single-particle excitations, and the recoil of individual atoms is observed. The boundary between these two regimes is not sharp, but rather smooth and continuous. Multiphonon scattering transforms into the recoil dispersion when Q becomes sufficiently large. Let us consider each case in turn.

To first approximation, the scattering at energy transfers between 100 meV and 200 meV is dominated by the incoherent one-phonon cross section of the hydrogen atoms. The reasons for this are twofold. First, the incoherent scattering cross section of H is approximately thirteen times larger than the total scattering cross section of Zr. Second, the intensity of optical modes is inversely proportional to the mass of the participating atoms. Since H is much lighter than Zr, there is a large relative gain in intensity for modes involving the H atoms. Neglecting multiphonon scattering, we may write the incoherent dynamic structure factor as follows [33]:

$$S^{(i)}(Q,E) \propto e^{-2W} \frac{\hbar^2 Q^2}{2m} \frac{G(E)}{E} (1 + n(E,T)) \tag{1}$$

Here e^{-2W} is the Debye-Waller factor, where $2W = Q^2\langle u^2\rangle$; $\langle u^2\rangle$ is the dynamic mean-squared displacement of the scattering atoms; m is the individual mass of those atoms; $G(E)$ is the generalized vibrational density of states; and $n(E,T) = (\exp(E/k_BT) - 1)^{-1}$ is the Bose population factor.

At high Q, the scattering may be described within the framework of the Impulse Approximation (IA) [23]. According to the IA, the kinetic energy transferred by an incident neutron to an individual hydrogen atom is so large that the potential energy of the hydrogen atom in both its initial and final states may be neglected. Intuitively, a high-energy neutron undergoes an impulsive collision with a single target atom, and this atom recoils freely from the impact. If the interparticle potential does not contain an infinitely hard core, then, in the limit $Q \to \infty$, $S^{(i)}(Q,E)$ reduces to an integral transform of the atomic momentum distribution $n(k)$:

$$S_{\mathrm{IA}}(Q,E) = \int n(\mathbf{k}) \delta \left(E - \frac{\hbar^2 Q^2}{2m} - \frac{\hbar^2 \mathbf{k}\cdot\mathbf{Q}}{m} \right) d\mathbf{k}. \tag{2}$$

A constant Q cut of the dynamic structure factor $S_{\mathrm{IA}}(Q,E)$ consists of a single symmetrical peak located at the recoil energy of hydrogen atom initially at rest, namely $\hbar^2Q^2/2m$. Due to the third term in the energy-conserving δ-function, the width of the peak is proportional to the product of Q and the width of $n(k)$.

While $n(k)$ can be inferred from the dynamic structure factor $S_{\mathrm{IA}}(Q,E)$, it is convenient to recast the data in terms of the West scaling variable Y and the neutron Compton profile $J(Y,Q)$. These quantities are defined as follows [23,35]:

$$Y = \frac{m}{\hbar^2 Q} \left(E - \frac{\hbar^2 Q^2}{2m} \right). \tag{3}$$

$$J(Y,Q) = \frac{\hbar^2 Q}{m} S(Q,E). \tag{4}$$

The West scaling variable Y has the physical interpretation of being the component $k_\parallel$ of the atomic momentum that is parallel to the momentum transfer $\mathbf{Q}$; that is, $k_\parallel = \mathbf{k}\cdot\hat{\mathbf{Q}}$. The neutron Compton profile is a one-dimensional projection of the momentum distribution, at least in the IA-limit:

$$\lim_{Q\to\infty} J(Y,Q) = J_{IA}(Y) = 2\pi \int_{|Y|}^{\infty} k n(k) dk. \tag{5}$$

The ω^2-sum rule of neutron scattering requires that the second moment of the neutron Compton profile be proportional to the average atomic kinetic energy $\langle E_K\rangle$:

$$\int_{-\infty}^{+\infty} Y^2 J(Y,Q) dY = \frac{2m}{3\hbar^2} \langle E_K \rangle \tag{6}$$

Accordingly, the average atomic kinetic energy $\langle E_K\rangle$ may be extracted from the intrinsic second-moment of the scattering.

3. Experimental procedure

3.1. Sample preparation and characterization

The Zircaloy 2 (Zy-2) material used for this study is a solid solution Zr–Sn binary alloy with Fe, Cr, and Ni added to promote corrosion resistance [36]. The composition of our Zy-2 material has been published previously [19]. The solubility of Fe, Cr, and Ni in Zr is very low and these elements form intermetallic second phase precipitates in Zr. Generally, the metal solutes do not influence hydrogen behavior. For example, Kearns demonstrated the hydrogen diffusivity is unaffected by alloy composition [37]. The local interatomic interaction potential likewise is not expected to be influenced by the trace solutes since these are at very low concentration, less than 0.1% by weight (for Fe, Cr, and Ni) and approximately 1% by weight for Sn. Thus, we believe our study of the vibrational modes and zero-point energy of hydrogen in Zy-2 and the comparison to ε-ZrH_2 is warranted.

Beta-quenched, un-recrystallized rolled Zircaloy 2 plate supplied by ATI Specialty Materials with a composition consistent with UNS R60802 specification [38] was used for the neutron scattering experiments described here. The as-received plate was 3.4 mm thick. Zircaloy 2 bars with a 4 mm by 3.4 mm cross section and 45 mm long were cut from the plate using electric discharge machining to avoid plastic deformation associated with mechanical cutting. All surfaces were mechanically abraded with 1200 grit paper to remove surface contamination and to facilitate hydrogen loading. The *in situ* neutron scattering temperature cycling employed here involved temperatures in excess of 750 K that would induce recrystallization. The sample material was therefore annealed in flowing Ar gas at 973 K for 6 h to ensure complete recrystallization prior to the neutron scattering measurements. The research purity (99.999% source gas) Ar gas stream was purified by a getter furnace upstream of the anneal furnace. Recystallization was confirmed using X-ray diffraction [19]. Additional details regarding sample characterization can be found in Ref. [19].

Hydrogen loading to a concentration of 170 μg/g (formula unit of $ZrH_{0.0155}$) was performed using a Sievert's apparatus described previously [39] by exposure of the sample material to H_2 gas at

Please cite this article as: T.R. Prisk et al., Vibrational modes and quantum zero-point energy of hydrogen in $ZrH_{0.0155}$ and ZrH_2, Journal of Alloys and Compounds, https://doi.org/10.1016/j.jallcom.2019.152832

673 K. Briefly, this system allows controlled exposure of materials (Zircaloy 2 in the present case) to hydrogen gas in a constant volume with accurate absolute pressure measurement in a stainless steel gas manifold. The measured pressure decreases as the specimen absorbs solute atoms. The ideal gas law can then be used to calculate the absorbed solute concentration once equilibrium is obtained for a given sample mass and the measured total pressure reduction. Gas pressure was monitored with four capacitance manometers spanning a pressure range from 10^5 Pa to 10^{-2} Pa. The total H_2 pressure change was 8666 Pa, corresponding to a hydrogen concentration of 170 μg/g calculated using the ideal gas law, the known volume of the Sievert's system (4.549 l), and the total sample mass (187 g). The sample material for the neutron scattering experiments presented here was identical to that published elsewhere [19] and the reader is directed to that publication for additional details.

The ZrH_2 sample was obtained from Sigma-Aldrich. It has 325 mesh (particle size smaller than 44 μm) and 99% purity. We performed X-ray powder diffraction measurements using Cu K-α radiation, confirming that the composition is ε-ZrH_2 (a = 4.980922(19) Å, c = 4.4482(2) Å, c/a = 0.893, space group $I4/mmm$) [40]. There was no evidence in the X-ray powder diffraction data for the presence of a δ-hydride phase or untransformed Zr in this sample.

3.2. Inelastic neutron scattering

We conducted an inelastic neutron scattering study of $ZrH_{0.0155}$ and ZrH_2 using the Fine-Resolution Fermi Chopper Spectrometer, also known as SEQUOIA [30,31]. This instrument is a direct geometry, time-of-flight spectrometer located at the Spallation Neutron Source. It will be briefly described here. The incident neutron flight path begins with a decoupled poisoned water moderator. The neutrons are transported through a parabolic focusing guide. A T_0-chopper is located 10.0 m from the moderator. This chopper reduces the background produced by the initial prompt pulse of neutrons and γ-rays emitted by the liquid mercury target. However, in order to access energies as high as 6.2 eV, the T_0-chopper is not fully closed at the time of the prompt pulse. The neutrons continue through the guides to a Fermi chopper located 18.0 m from the moderator. The incident neutron energy is chosen by the phase of this chopper relative to the pulse. For this work, we employed a Fermi chopper having 100 mm long slit package, 33 slits of 1.5 mm width, 0.35 mm thick absorbing slats, and a radius of curvature of 1.83 m. When performing measurements with an incident neutron energy E_i of (200 meV, 350 meV, 500 meV, 800 meV, and 6200 meV), we operated the Fermi chopper with respective frequencies (360 Hz, 360 Hz, 480 Hz, 600 Hz, and 600 Hz) and the T_0-chopper with respective frequencies (120 Hz, 120 Hz, 150 Hz, 180 Hz, and 180 Hz). All of these chopper settings were used to study $ZrH_{0.0155}$, but only the 200 meV and 6.2 eV incident energies were used with ZrH_2. The resolution width is a function of Fermi chopper frequency, incident neutron energy E_i, and the energy transfer E. Calculations of the resolution width are described in the Appendix. Python code for evaluating the (inelastic) energy resolution is available through an online repository [41].

The sample environment, described below, is located 20 m from the moderator. The secondary flight path of SEQUOIA is comprised of a cylindrical detector bank, centered on the sample environment, with position-sensitive ^{3}He detectors. They span $-30^\circ \leq \varphi \leq 60^\circ$ in the horizontal plane and ±18° vertically. Two low efficiency beam monitors are located 18.26 m and 29.0 m from the moderator. The beam profile observed at these monitors is used to determine the neutron energy E_i and moderator emission time t_0, quantities necessary for transforming the observed double-differential scattering cross section $d^2\sigma/d\Omega dt_f$ to the dynamic structure factor $S(Q,E)$. The data was reduced using Mantid [42] and analyzed with DAVE [43]. We have not attempted to put the scattering on an absolute intensity scale (i.e. in units of 1/meV). We will present the scattering intensity in arbitrary units throughout the paper.

We placed 59.67 g of $ZrH_{0.0155}$ bars into a 0.4 cm thick plate-shaped sample cell and oriented the bar surfaces normal to the incident neutron beam. We expect approximately 90% transmission from this sample geometry, as the bound macroscopic scattering cross section of Zr with a density of 6.5 g/cc is 0.28 cm^{-1}. In the same geometry, we measured 59.61 g of Zr bars containing no hydrogen. The beam size was set to 5.0 cm by 5.0 cm and the remainder of the sample cell was shielded by boron nitride. We loaded the ZrH_2 powder (m = 1.526 g) into a flat aluminum cell of 0.1 mm thickness. A lower limit for the ZrH_2 sample transmission can be estimated to be approximately 96%. Given these transmission estimates, we assume that multiple scattering makes a negligible contribution to the observed scattering for the three samples, Zr, ZrH_2, $ZrH_{0.0155}$. A top-loading closed-cycle refrigerator was used for the $ZrH_{0.0155}$ measurements, whereas a bottom-loading closed-cycle refrigerator was used for the ZrH_2 measurements.

Measurements were carried out on the $ZrH_{0.0155}$ sample in the following sequence: 6.0 K, 550 K, and 617 K. At 6.0 K, nearly all of the hydrogen atoms may be found in the δ phase. However, at higher temperatures, the α and δ phases co-exist. We estimate that the mole fraction of hydrogen in the solid solution α-phase is approximately 23% at 550 K and 59% at 617 K.

4. Results

Fig. 3 illustrates the dynamic structure factor $S(Q,E)$ of $ZrH_{0.0155}$ at 6.0 K. Acoustic phonons are observed at energies below ≈30 meV. The fundamental optical modes appear as a dispersionless band located at 140 meV. Beyond these fundamental modes, there is a series of unevenly spaced, dispersionless bands corresponding to the higher oscillator states of the hydrogen atoms. At 6.2 eV incident energy, the recoil dispersion of the hydrogen atoms is observed.

Fig. 4 compares the inelastic scattering function of $ZrH_{0.0155}$ and ZrH_2 at 6.0 K. Although two different hydride phases exist within these samples, namely the δ-$ZrH_{1.6}$ phase in $ZrH_{0.0155}$ and the ε phase in ZrH_2, their inelastic scattering functions $S(E)$ are qualitatively similar. The scattering from the δ-hydride precipitates may be regarded as showing bulk dynamics, as the δ-hydride particles are greater than 1μm in size [44]. As can be seen, the observed oscillator transitions occur at nearly the same energies. However, a broadening of these peaks is observed in $ZrH_{0.0155}$. This is likely due to the fact that the vacancies on the H sublattice are disordered in the δ-hydride. In particular, hydrogen atoms randomly occupy only 80% of available positions in the fcc fluorite-type ($Fm\bar{3}m$) lattice. One expects a larger distribution of H–H nearest neighbor distances in the non-stoichiometric δ-hydride than the fully ordered ε-ZrH_2.

The inelastic scattering function $S(E)$ in the region of the fundamental optical modes (100 meV–190 meV) is shown in Fig. 4 (a). Four distinct transitions are observed in ZrH_2 at 134 meV, 138 meV, 146 meV, and 156 meV. This result is consistent with previous measurements [45]. These four modes are also present in the δ-hydride of $ZrH_{0.0155}$, apart from a shift in energy and an

Please cite this article as: T.R. Prisk et al., Vibrational modes and quantum zero-point energy of hydrogen in $ZrH_{0.0155}$ and ZrH_2, Journal of Alloys and Compounds, https://doi.org/10.1016/j.jallcom.2019.152832

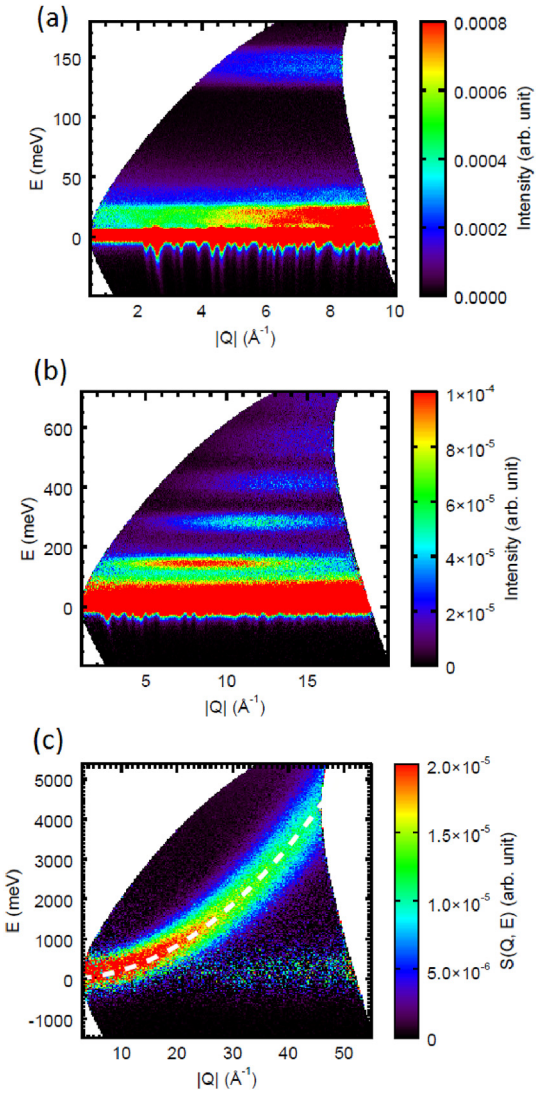

Fig. 3. The dynamic structure factor $S(Q, E)$ of $ZrH_{0.0155}$ at 6.0 K. Measurements were performed with the SEQUOIA spectrometer using incident neutron energies of (a) 200 meV, (b) 800 meV, and (c) 6200 meV. In panel (c), the scattering from the zirconium has been subtracted and the dashed white line indicates the recoil dispersion of atomic hydrogen.

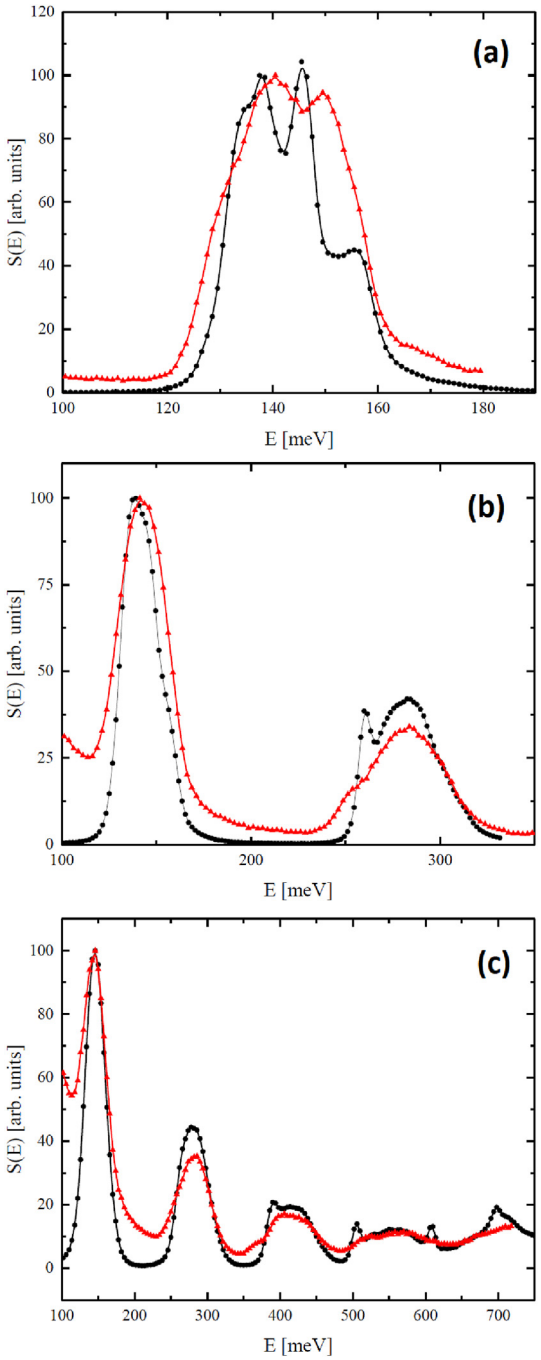

Fig. 4. The inelastic scattering functions $S(E)$ of ZrH_2 (black circles) and $ZrH_{0.0155}$ (red triangles) at 6.0 K. The incident neutron energies used to obtain the data shown in panels (a), (b), and (c) are 200 meV, 350 meV, and 800 meV, respectively. The resolution width in panel (a) at 140 meV is 1.8 meV. In panel (b), the resolution width is 6.2 meV and 3.1 meV at 140 meV and 280 meV energy transfers, respectively. Error bars are smaller than symbol sizes.

increase of the intrinsic width. By inspection, the new peak positions are: 130 meV, 140 meV, 151 meV, and 157 meV. The extent of the broadening is difficult to determine as these four peaks significantly overlap. The feature near 165 meV in the INS spectra of both samples is likely a combination mode comprised of acoustic phonons and optical vibrations.

Fig. 4 (b) illustrates the inelastic scattering function $S(E)$ at energies between 100 meV and 350 meV. The fine structure of the fundamental optical modes is washed out by the instrumental energy resolution and so only a single peak appears in the scattering. This peak is located at 139 meV and 141 meV in ZrH_2 and $ZrH_{0.0155}$, respectively. A breakdown of the harmonic approximation is evident from the data. In the two-phonon band, sharp peaks are observed at 260 meV and 253 meV for ZrH_2 and $ZrH_{0.0155}$, respectively. These peaks are the first overtones of the transitions located at 134 meV and 130 meV. If these systems were perfectly harmonic and isotropic, then these overtones would occur at exactly twice the energy of the fundamental mode, namely 268 meV and 260 meV. The remainder of the two-phonon band is peaked near 283 meV in both materials.

Fig. 4 (c) plots the observed scattering between 100 meV and 750 meV. The broad peak in the three-phonon band is centered near 418 meV. A low energy shoulder is located at 386 meV and

Please cite this article as: T.R. Prisk et al., Vibrational modes and quantum zero-point energy of hydrogen in $ZrH_{0.0155}$ and ZrH_2, Journal of Alloys and Compounds, https://doi.org/10.1016/j.jallcom.2019.152832

366 meV in ZrH_2 and $ZrH_{0.0155}$, respectively. This peak is the second overtone of the lowest fundamental mode. These peaks would occur at 402 meV and 390 meV were the harmonic approximation correct. The difference between the observed peak energy and the harmonic approximation is 16 meV in ZrH_2 and 24 meV in $ZrH_{0.0155}$, indicating greater anharmonicity in the $ZrH_{0.0155}$ sample.

The four-phonon band has a broad peak centered approximately at 560 meV. In ZrH_2, sharp peaks occur at 506 meV and 610 meV. While the 506 meV peak may be assigned to the third overtone of the fundamental optical peak, it does not occur at 536 meV as the harmonic approximation would require. The higher overtones are too broadened to determine their detailed positions. The observed anharmonicity in ZrH_2 is in good agreement with the total-energy calculations of Ref [16], which reports that the hydrogen potential in ε-ZrH_2 is harmonic at low energies and becomes anharmonic at energies above 300 meV.

5. Discussion

5.1. Vibrational density of states

In order to determine the generalized vibrational density of states $G(E)$, we applied Equation (1) to the observed dynamic structure factor $S(Q,E)$. The mean-squared displacement $\langle u^2 \rangle$ was estimated from the $E_i = 500$ meV measurements. The dynamic structure factor $S(Q,E)$ was initially transformed into $G(E)$ under the assumption that $\langle u^2 \rangle = 0.0$ Å^2. The fundamental optical peak was fit to a single Gaussian and the integrated intensity was obtained as a function of Q, allowing for an estimate of $\langle u^2 \rangle$. We find that $\langle u^2 \rangle = 0.015$ Å^2 at all temperatures.

The generalized vibrational density of states $G(E)$ vs E is shown in Fig. 5. The fine structure in the $G(E)$ of $ZrH_{0.0155}$ is lost as the temperature increases. The asymmetrical, triangular shape of $G(E)$ at 617 K is similar to that found in $ZrH_{0.05}$ at 873 K [46]. At 617 K, the fundamental peak extends to low energies, approaching the phonons of the Zr lattice. Part of the increase of $G(E)$ below 120 meV is due to the multiphonon processes of α-Zr. However, it seems unlikely that the large increase of $G(E)$ down to 60 meV can be accounted for by these proceses alone. Instead, we suspect that the redistribution of intensity toward lower energies is at least partly due to the diffusion of hydrogen at these temperatures. The self-diffusion constant of H through Zr-alloys is of order 10^{-7} cm^2/s to 10^{-6} cm^2/s at temperatures between 570 K and 670 K [19,37,47]. Hon [48] and Majer et al. [49] suggest that, while moving from one tetrahedral site to another, hydrogen passes through octahedral sites. The octahedral interstices in hcp and fcc lattices are larger than their tetrahedral counterparts, thereby softening the fundamental modes [50]. For example, the fundamental optical mode of face-centered orthorhombic $TiH_{0.71}$, with hydrogen on octahedral sites, has an energy of 75 meV. In contrast, in other Ti–H hydrides where H occupies tetrahedral positions, the fundamental peak is in the range 140 meV–160 meV. Therefore, we suggest that the observation of additional intensity in the INS spectrum of α-$ZrH_{0.0155}$ at high temperatures is connected to the passage of hydrogen through octrahedral positions. The quasi-elastic neutron scattering data which is presently available [19] does not extend to sufficiently high Q to probe elementary diffusion steps, and so a conclusive statement cannot be made at this time.

The phonon dispersion curves of ε-ZrH_x have been calculated from first principles [51,52] and the predicted spectra are in good

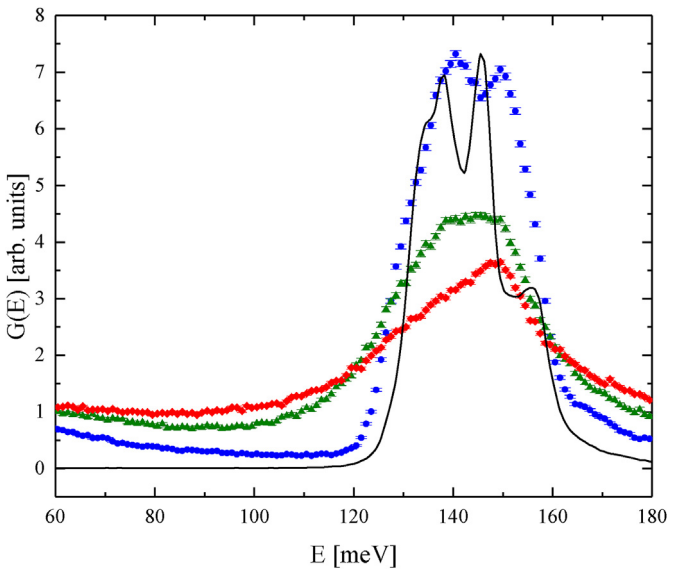

Fig. 5. The generalized vibrational density of states of ZrH_2 (black line) at 6.0 K and $ZrH_{0.0155}$ at 6.0 K (blue circles), 550 K (green triangles), 617 K (red diamonds). The plotted symbols share a common intensity scale; the solid black curve has been scaled for ease of comparison.

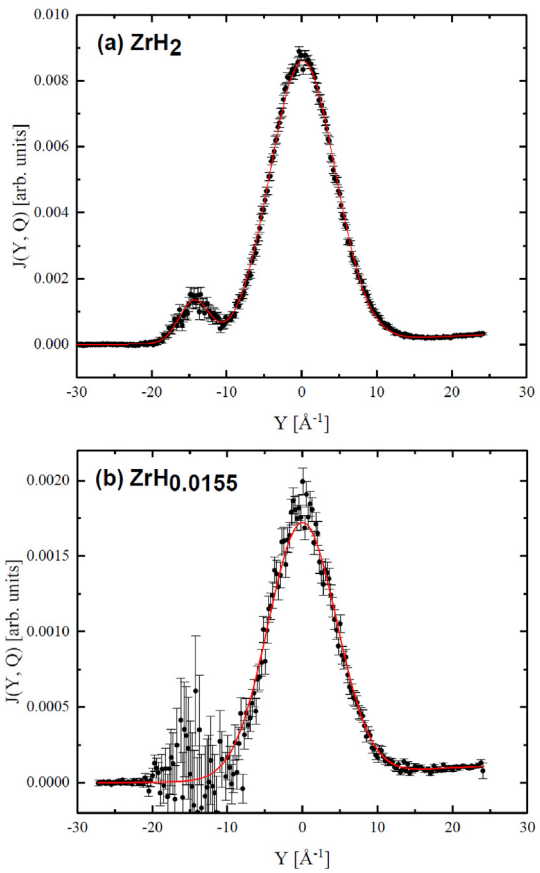

Fig. 6. The neutron Compton profile $J(Y,Q)$ of the hydrogen atoms in (a) ZrH_2 and (b) $ZrH_{0.0155}$ at 6.0 K. The scattering from the zirconium has been subtracted from the data shown in panel (b) but not from the data shown in panel (a). The solid red curve represents a model fit as described in the main text. Error bars throughout the paper represent one standard deviation, unless stated otherwise.

Please cite this article as: T.R. Prisk et al., Vibrational modes and quantum zero-point energy of hydrogen in $ZrH_{0.0155}$ and ZrH_2, Journal of Alloys and Compounds, https://doi.org/10.1016/j.jallcom.2019.152832

agreement with the experimental spectra. At room temperature, hydrogen in the phases studied here have Zr–H distances of 2.070 Å in fcc δ-$ZrH_{1.6}$, 2.083 Å in fct ε-ZrH_2, and 2.055 Å in hcp α-Zr. In other words, the nearest Zr–H distances decreases with phase in the following manner: $\varepsilon \rightarrow \delta \rightarrow \alpha$. As the temperature increases, more H goes into the solid solution α-ZrH_x phase with smaller Zr–H distance. This "hardens" $G(E)$ in the low H-concentration data.

The fine structure of the fundamental peak in ε-ZrH_2 can be explained by tetragonal distortion of the tetrahedral lattice site and dispersion of the optic phonon modes is due to strong H–H interactions. The fundamental peak of δ-$ZrH_{1.6}$ is less structured than that in ε-ZrH_2. This is due to the disordered hydrogen sublattice, where the H lattice sites on average have cubic symmetry. Further broadening of the fundamental peak in α-ZrH_x ($x < 0.009$) at high temperature is presumably due to the shorter occupancy time of hydrogen positions and the large diffusion of hydrogen through the material, as suggested above.

5.2. Proton momentum distribution

Fig. 6 shows the neutron Compton profile $J(Y,Q)$ at $Q = 28$ Å^{-1}. In ZrH_2, the measured scattering consists of three different contributions to the signal: the recoil of hydrogen atoms produces a peak located at $Y = 0$ with a full-width at half-maximum (FWHM) of ≈10 Å^{-1}; scattering from Zr produces a smaller peak located at $Y = -15$ Å^{-1}; and finally there is a high-energy tail due the transmission of unmoderated, fast neutrons through the spectrometer [22]. The same features are observed in the scattering from $ZrH_{0.0155}$. In this case, we have performed separate measurements of the scattering from zero hydrogen concentration Zircaloy-2 rods and subtracted this signal from the $ZrH_{0.0155}$ data set.

We assume that the hydrogen atoms can be understood as single particles moving in an effective external potential. At zero temperature, the momentum distribution $n(k)$ of these particles is determined solely by the ground state wavefunction. At finite temperatures, the momentum distribution is determined by a mixture of different wavefuctions, each appropriately weighted according to the canonical distribution of statistical mechanics. Given the level spacing of ≈ 140 meV, only the ground state and the lowest excited states contribute significantly to $n(k)$ at the temperatures considered here. We adopt a Gaussian model of the momentum distribution:

$$n(k) = \frac{1}{(2\pi\sigma^2)^{3/2}} e^{-k^2/2\sigma^2} \tag{7}$$

where the second moment σ^2 is an unknown parameter to be determined by a least-squares fit to the scattering data. According to Equation (5), the IA-scattering also assumes the following form:

$$J_{IA}(Y) = \frac{1}{\sqrt{2\pi\sigma^2}} e^{-Y^2/2\sigma^2} \tag{8}$$

We fit the observed $J(Y,Q)$ from ZrH_2 to a sum of three Gaussians, representing the neutron Compton profile of H, the fast neutron background at high energy, and the signal from the Zr atoms. This last term was not included in the model when fitting the $ZrH_{0.0155}$ data sets as the scattering from Zr was separately measured and subtracted from the raw data. In particular, the neutron Compton profile $J(Y,Q)$ was broken into sixteen groups for 25.0 Å^{-1} ≤ Q ≤ 40.0 Å^{-1}. These sixteen groups were simultaneously fit so that the best estimate of σ is determined by all values of Q at once. The model fit function was convoluted with the instrumental resolution function $I(Y,Q)$ at each value of Q. We found that the Gaussian model yielded a good fit at all temperatures and that our data does not provide a statistical justification for adopting a non-Gaussian model for $n(k)$.

Table 1
Proton Kinetic Energies in Metal Hydrides

Material	T [K]	$\langle E_K \rangle$ [meV]	Source
ZrH_2	6.0	109.0±0.3	Present Work
ZrH_2	20	112±2	Ref [15]
ZrH_2	290	108.0±0.5	Ref [15]
$ZrH_{0.0155}$	6.0	112.9±1.4	Present Work
$ZrH_{0.0155}$	550	119.4±1.4	Present Work
$ZrH_{0.0155}$	617	118.3±1.4	Present Work
NbH	20	122±3	Ref [15]
NbH	290	115.6±1.6	Ref [15]
TiH_2	20	115±2	Ref [15]
TiH_2	290	114±2	Ref [15]
CaH_2	20	83.3±1.4	Ref [15]
CaH_2	290	88.4±1.9	Ref [15]
NaH	20	66.3±0.9	Ref [60]
LiH	20	80±1	Ref [60]
LiH	20	73.8±0.3	Ref [60]
NaH	20	66.9±0.4	Ref [61]
KH	20	57.7±0.4	Ref [61]
RbH	20	55.0±0.2	Ref [61]
CsH	20	51.3±0.2	Ref [61]

Empirical estimates of the proton kinetic energy $\langle E_K \rangle$ in various metal hydrides are listed in Table 1. There is good agreement between our empirical estimate of the proton kinetic energy in ZrH_2 and the value reported in Refs. [14,15]. The proton kinetic energy in the δ-hydride phase of $ZrH_{0.0155}$ is 112.9±1.4 meV, slightly higher than its value in the ε-phase of ZrH_2, namely 109.0±0.3 meV. As the temperature increases from 6.0 K to 550 K and 617 K, the average proton kinetic energy $\langle E_K \rangle$ of $ZrH_{0.0155}$ increases by approximately 5%.

6. Conclusions

In this paper, we presented measurements of the inelastic scattering function $S(E)$, generalized density of states $G(E)$, and average proton kinetic energy $\langle E_K \rangle$ of ZrH_2 and $ZrH_{0.0155}$. In general, our results are in good agreement with previous inelastic neutron scattering studies of ZrH_2, including the determination of the average proton kinetic energy and the spectrum of optical modes. The new data set was obtained with a state-of-the-art neutron spectrometer, SEQUOIA. The source strength allowed for high-precision and high-resolution measurements, not only on the ZrH_2 sample, but also the much lower concentration $ZrH_{0.0155}$ sample. Previous neutron Compton scattering studies of proton momentum distributions have been restricted only to resonance-foil spectrometers; here we demonstrated the usefulness of direct geometry spectrometers to examine proton momentum distributions.

At low temperatures, the two samples form two different hydride phases, ε-ZrH_2 and α-Zr + δ-$ZrH_{1.6}$. We find that the fundamental optical mode of ε-ZrH_2 is split by tetragonal distortions of the lattice and strong H–H interactions. In $ZrH_{0.0155}$, the fundamental optical peak and higher energy transitions are broadened by disorder in the hydrogen sublattice. Evidence of anharmonicity is present in both samples: the overtones of the optical peaks are shifted from their expected positions in the harmonic approximation.

Please cite this article as: T.R. Prisk et al., Vibrational modes and quantum zero-point energy of hydrogen in $ZrH_{0.0155}$ and ZrH_2, Journal of Alloys and Compounds, https://doi.org/10.1016/j.jallcom.2019.152832

Our data is broadly consistent with the theoretical predictions of Ref [16], where it is argued that the effective potential experienced by the H atoms in Zr is nearly isotropic and harmonic below 300 meV, but anisotropic and anharmonic at higher energies. We find that the momentum distribution $n(k)$ is Gaussian, which is consistent with the prediction that the potential well is approximately harmonic for small displacements of the hydrogen atoms. Given the size of the level spacings, $n(k)$ is governed primarily by the ground state wavefunction and secondarily by the first excited state. The anharmonicity of the potential only becomes evident for higher excited states, which do not contribute significantly to $n(k)$ at the temperatures considered here.

Acknowledgements

The authors gratefully acknowledge helpful scientific discussions with Richard T. Azuah. This work was performed with support from the US Department of Energy Nuclear Energy University Programs Integrated Research Project under contract number IRP-12-4728 (DE-00131989). A portion of this work was performed at the Frederick Seitz Materials Research Laboratory Central Facilities, University of Illinois and this is gratefully acknowledged. This research used resources at the Spallation Neutron Source, a DOE Office of Science User Facility operated by Oak Ridge National Laboratory. Certain commercial equipment, instruments, or materials are identified in this paper in order to specify the experimental procedure adequately. This identification is not intended to imply recommendation or endorsement by the National Institute of Standards and Technology. The data sets reported in the present paper are available from the authors upon reasonable request.

Appendix A. Instrumental Resolution

In order to obtain accurate empirical estimates of $n(k)$ and $\langle E_K \rangle$, one must account for the effects of the instrumental resolution function $I(Y,Q)$ upon the experimental neutron Compton profile $J_{EXP}(Y,Q)$. In general, the (inelastic) resolution function of a time-of-flight spectrometer at a spallation neutron source assumes an asymmetric shape. This is due to the fact that the neutron pulses have a complex velocity and time distribution determined by the target and moderator system [33]. In this case, it is appropriate to adopt a Gaussian approximation wherein the contributions to the energy resolution δE from the moderator pulse width dt_m, the Fermi chopper pulse width dt_c, and the detector time uncertainty dt_d combine in quadrature [30,53,54]. In particular, the inelastic energy resolution is given by the following expression:

$$\delta E = m_n \sqrt{\left(\frac{v_i^3}{L_0} + v_f^3 \frac{L_1}{L_0 L_2}\right)^2 dt_m^2 + \left(\frac{v_i^3}{L_0} + v_f^3 \frac{L_0 + L_1}{L_0 L_2}\right)^2 dt_c^2 + \left(\frac{v_f^3}{L_2}\right)^2 dt_d^2} \tag{A.1}$$

Here m_n is the mass of the neutron; v_i and v_f are the nominal initial and final velocities of the neutron, respectively; L_0 is the moderator to Fermi chopper distance; L_1 is the distance between the Fermi chopper and the sample position; and L_2 is the distance from the sample to the detectors. We obtained the moderator pulse width dt_m from Monte Carlo *N*-Particle Transport Code System (MCNPX) simulations of the decoupled water moderator [55]. The observed profile width in the first beam monitor was taken as an estimate of dt_c. The detector time uncertainty dt_d is given by the width of a detector divided by the neutron final velocity v_f.

To verify the appropriateness of this approximation, as well as the incident neutron energy E_i used in the data reduction, we performed a ray-tracing Monte Carlo simulation of the SEQUOIA incident flight path with the McStas software suite [56,57]. The results of the simulation are compared to experimental data in Fig. A1. There is excellent agreement between the observed and predicted monitor spectra. This confirms that our estimates of dt_m and E_i are correct. The simulated curves are shifted by 2 μs to account for delays in the experimental timing chain, e.g. cable length effects [30,31]. We point out that Monitor 2 is particularly sensitive to the description of the moderator. In addition, the profile shapes indicate that it is appropriate to adopt a Gaussian approximation for the resolution lineshape.

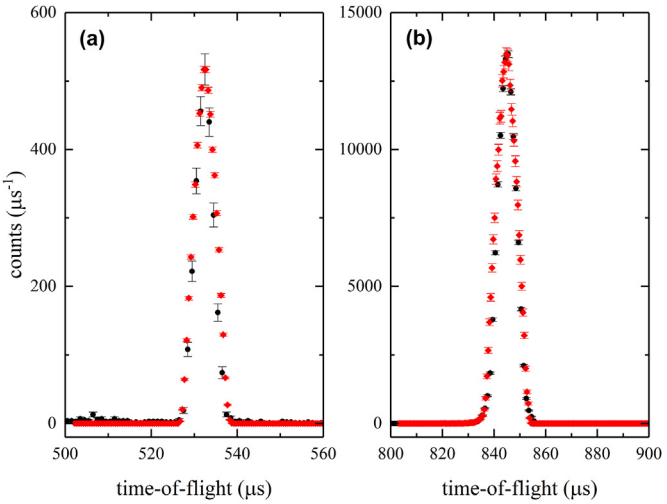

Fig. A.1. The time-of-flight spectra of (a) Monitor 1, located just after the Fermi chopper, and (b) Monitor 2, which is located just before the beam stop. Black circles are experimental points and red diamonds are from the Monte Carlo simulation. The simulated points have been shifted to the right by 2 μs to account for differences between the observed and predicted t_0 and rescaled vertically to allow for a direct visual comparison. Error bars on the experimental points are given by Poisson counting statistics.

The observed neutron Compton profile $J_{EXP}(Y,Q)$ is obtained by convoluting the intrinsic scattering with the instrumental resolution function $I(Y,Q)$:

$$J_{EXP}(Y,Q) = \int_{-\infty}^{+\infty} J_{IA}(Y') I(Y - Y', Q) dY' \tag{A.2}$$

The instrumental resolution function $I(Y,Q)$ is represented by a single Gaussian in *Y*. The full-width at half-maximum of $I(Y,Q)$ decreases smoothly from 3.93 Å^{-1} at $Q = 25.0$ Å^{-1} to 1.54 Å^{-1} at $Q = 40.0$ Å^{-1}.

Appendix B. Elastic and Acoustic Phonon Scattering

Fig. B1 compares the inelastic scattering function $S(E)$ from $ZrH_{0.0155}$ and ZrH_2 at energies between −50 meV and 175 meV. The spectrum of ZrH_2 has been plotted with two different scale factors: the black points approximately match the $ZrH_{0.0155}$ intensity (red points) at 140 meV, while the blue points approximately match the $ZrH_{0.0155}$ intensity at 20 meV. The scattering from acoustic phonons is not well-separated from the diffraction peaks as the elastic energy resolution is approximately 4.5 meV.

Please cite this article as: T.R. Prisk et al., Vibrational modes and quantum zero-point energy of hydrogen in $ZrH_{0.0155}$ and ZrH_2, Journal of Alloys and Compounds, https://doi.org/10.1016/j.jallcom.2019.152832

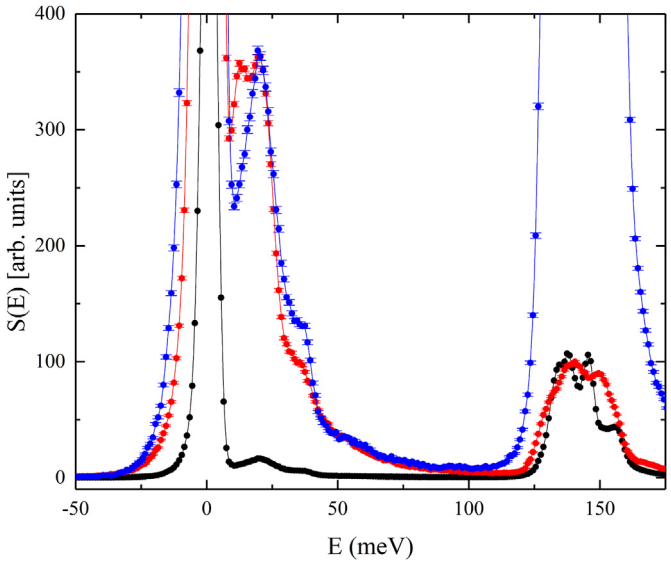

Fig. B.1. The inelastic scattering function $S(E)$ of $ZrH_{0.0155}$ and ZrH_2 at 6.0 K are compared. The red points designate the scattering from $ZrH_{0.0155}$ at a temperature of 6.0 K. The blue points plot the scattering from ZrH_2, but appropriately scaled to permit a comparison with $ZrH_{0.0155}$ below 50 meV. The black points illustrate the same data set, but scaled so as to permit a comparison in the range of the optical modes near 140 meV. The scattering from the aluminum sample holder has not been subtracted from the data.

The spectra of the $ZrH_{0.0155}$ and ZrH_2 are similar up to 100 meV, at least within this coarse energy resolution. The most pronounced difference is the relative intensity of the acoustic modes and the fundamental optical modes. This difference may be understood, at least in part, as stemming from the molar fraction of each type of atom as well as the neutron scattering cross section divided by the atomic mass σ/m. In ZrH_2, there are 133 times more H atoms per Zr atom than in the $ZrH_{0.0155}$ sample. In addition, the "strength" of the scattering from H is much larger than the "strength" of the scattering from Zr due to the ratio σ/m, where $\sigma/m = 0.071$ barns/amu for Zr and 81.4 b/amu for H. Therefore, one expects that the low energy modes in ZrH_2 will be weak in comparison with the optical modes.

References

[1] R.L. Williamson, J.D. Hales, S.R. Novascone, M.R. Tonks, D.R. Gaston, C.J. Permann, D. Andrs, R.C. Martineau, J. Nucl. Mater. 423 (2012) 149–163.
[2] A.T. Motta, A. Couet, R.J. Comstock, Annu. Rev. 45 (2015) 311–343.
[3] K. Une, S. Ishimoto, J. Nucl. Mater. 322 (2003) 66–72.
[4] M.P. Puls, Metall. Trans. A 21 (1990) 2905–2917.
[5] T. Zhang, R. Yue, X. Wang, Z. Hao, Nucl. Eng. Des. 330 (2018) 463–479.
[6] J. Bair, M.A. Zaeem, M. Tonks, J. Nucl. Mater. 466 (2015) 12–20.
[7] A.T. Motta, L. Capolungo, L.-Q. Chen, M.N. Cinbiz, M.R. Daymond, D.A. Koss, E. Lacroix, G. Pastore, P.-C.A. Simon, M.R. Tonks, B.D. Wirth, M.A. Zikry, J. Nucl. Mater. 518 (2019) 440–460.
[8] E. Zuzek, J.P. Abriata, A. San-Martin, F.D. Manchester, Bull. Alloy Phase Diagrams 11 (1990) 385–395.
[9] T. Springer, D. Richter, Hydrogen in metals, in: D.L. Price, K. Sköld (Eds.), Methods of Experimental Physics, 23 B, Academic Press, San Diego, CA, 1987, pp. 131–186.
[10] R. Hempelmann, J. Less Common. Met. 101 (1984) 69–96.
[11] S. Ikeda, N. Watanabe, K. Kai, Physica 120B (1983) 131–135.
[12] S. Ikeda, N. Watanabe, J. Phys. Soc. Jpn. 56 (1987) 565–576.
[13] S. Ikeda, M. Furusaka, T. Fukunaga, A.D. Taylor, J. Phys. Condens. Matter 2 (1990) 4675–4684.
[14] A.C. Evans, D.N. Timms, J. Mayers, S.M. Bennington, Phys. Rev. B 53 (1996) 3023–3031.
[15] A.C. Evans, J. Mayers, D.N. Timms, M.J. Cooper, Z. Naturforschung 48a (1993) 425–432.
[16] C. Elsässer, S. Schweizer, M. Fähnle, Mater. Res. Soc. Symp. Proc. 453 (1997) 221–226.
[17] A.A. Aczel, G.E. Granroth, G.J. MacDougall, W.J.L. Buyers, D.L. Abernathy, G.D. Samolyuk, G.M. Stocks, S.E. Nagler, Nat. Commun. 3 (2012) 1124.
[18] J.Y.Y. Lin, A.A. Aczel, D.L. Abernathy, S.E. Nagler, W.J.L. Buyers, G.E. Granroth, Phys. Rev. B 89 (2014) 144302.
[19] B.J. Heuser, T.R. Prisk, J.-l. Lin, T.J. Dax, Y. Zhang, J. Nucl. Mater. 518 (2019) 177–189.
[20] C. Andreani, D. Colognesi, J. Mayers, G.F. Reiter, R. Senesi, Adv. Phys. 54 (2005) 377–469.
[21] C. Andreani, M. Krzystyniak, G. Romanelli, R. Senesi, F. Fernandez-Alonso, Adv. Phys. 66 (2017) 1–73.
[22] R. Senesi, A.I. Kolesnikov, C. Andreani, J. Phys. Conf. Ser. 571 (2014), 012007.
[23] R.N. Silver, P.E. Sokol, Momentum Distributions, Plenum Press, New York and London, 1989.
[24] W.M. Snow, Y. Wang, P.E. Sokol, Europhys. Lett. 19 (1992) 403–408.
[25] H.R. Glyde, R.T. Azuah, W.G. Stirling, Phys. Rev. B 62 (2000) 14337.
[26] T.R. Prisk, M.S. Bryan, P.E. Sokol, G.E. Granroth, S. Moroni, M. Boninsegni, J. Low Temp. Phys. 189 (2017) 158–184.
[27] M.S. Bryan, T.R. Prisk, R.T. Azuah, W.G. Stirling, P.E. Sokol, Europhys. Lett. 115 (2016) 66001.
[28] W. Langel, D.L. Price, R.O. Simmons, P.E. Sokol, Phys. Rev. B 38 (1988) 11275.
[29] R.T. Azuah, W.G. Stirling, H.R. Glyde, M. Boninsegni, J. Low Temp. Phys. 109 (1997) 287–308.
[30] G.E. Granroth, A.I. Kolesnikov, T.E. Sherline, J.P. Clancy, K.A. Ross, J.P.C. Ruff, B.D. Gaulin, S.E. Nagler, J. Phys. Conf. Ser. 251 (2010) 012058.
[31] M.B. Stone, J.L. Niedziela, D.L. Abernathy, L. DeBeer-Schmitt, G. Ehlers, O. Garlea, G.E. Granroth, M. Graves-Brook, A.I. Kolesnikov, A. Podlesnyak, B. Winn, Rev. Sci. Instrum. 85 (2014) 045113.
[32] T.E. Mason, D. Abernathy, I. Anderson, J. Ankner, T. Egami, G. Ehlers, A. Ekkebus, G. Granroth, M. Hagen, K. Herwig, J. Hodges, C. Hoffmann, C. Horak, L. Horton, F. Klose, J. Larese, A. Mesecar, D. Myles, J. Neuefeind, M. Ohl, C. Tulk, X.-L. Wang, J. Zhao, Phys. B Condens. Matter 385 (2006) 955–960.
[33] C.-K. Loong, J.M. Carpenter, Elements of Slow-Neutron Scattering: Basics, Techniques, and Applications, Cambridge University Press, 2015.
[34] P.C.H. Mitchell, S.F. Parker, A.J. Ramirez-Cuesta, Vibrational Spectroscopy with Neutrons: with Applications in Chemistry, Biology, Materials Sciecne and Catalysis, Neutron Techniques and Applications, World Scientific, 2005.
[35] V.F. Sears, Phys. Rev. B 30 (1984) 44–51.
[36] J.L. Lin, X. Han, B.J. Heuser, J.D. Almer, J. Nucl. Mater. 471 (2016) 299–307.
[37] J.J. Kearns, J. Nucl. Mater. 43 (1972) 330–338.
[38] ASTM International Standard B351/B351M-13, Standard Specification for Hot-Rolled and Cold-Finished Zirconium and Zirconium Alloy Bars, Rod, and Wire for Nuclear Application, 2018.
[39] W.C. Chen, B.J. Heuser, J. Alloy. Comp. 312 (2000) 176–180.
[40] R.C. Bowman, B.D. Craft, J.S. Cantrell, E.L. Venturini, Phys. Rev. B 31 (1985) 5604.
[41] G.E. Granroth [link]. URL, https://github.com/granrothge/Resolution_Planner.
[42] O. Arnold, J.C. Bilheux, J.M. Borreguero, A. Buts, S. Cambell, L. Chapon, M. Coucet, N. Draper, R. Ferraz Leal, M.A. Gigg, V. Lynch, A. Markvardsen, D.J. Mikkelson, R.L. Mikkelson, R. Miller, K. Palmen, P. Parker, G. Passos, T. Perring, P. Peterson, S. Ren, M.A. Reuter, A.T. Savici, J.W. Taylor, R.J. Taylor, R. Tolchenov, W. Zhou, J. Zikovsky, Nucl. Instrum. Methods Phys. Res. A 764 (2014) 156–166.
[43] R.T. Azuah, L.R. Kneller, Y. Qiu, P.L.W. Tregenna-Piggott, C.M. Brown, J.R.D. Copley, R.M. Dimeo, J. Res. Natl. Inst. Stan. Technol. 114 (2009) 341.
[44] B.J. Heuser, J.-L. Lin, C. Do, L. He, J. Appl. Crystallogr. 51 (2018) 768–780.
[45] J.G. Couch, O.K. Harling, L.C. Clune, Phys. Rev. B 4 (1971) 2675–2681.
[46] R. Khoda-Bakhsh, D.K. Ross, J. Phys. F Met. Phys. 12 (1982) 15–24.
[47] Y. Zhang, C. Jiang, X. Bai, Sci. Rep. 7 (2017) 41033.
[48] J.F. Hon, J. Chem. Phys. 36 (1962) 759–763.
[49] G. Majer, W. Renz, R.G. Barnes, J. Phys. Condens. Matter 6 (1994) 2935–2942.
[50] A.I. Kolesnikov, V.K. Fedotov, I. Natkanets, S. Khabrylo, I.O. Bashkin, E.G. Polyatovskii, JETP Lett. (Engl. Transl.) 44 (1986) 509–512.
[51] P. Zhang, B.-T. Wang, C.-H. He, P. Zhang, Comput. Mater. Sci. 50 (2011) 3297–3302.
[52] D. Chattaraj, S.C. Parida, S. Dash, C. Majumder, Int. J. Hydrogen Energy 39 (2014) 9681–9689.
[53] R.K. Crawford, General principles of time-of flight scattering instrument design, in: J.M. Carpenter, D.L. Price, N.J. Swanson (Eds.), IPNS A National Facility for Condensed Matter Research, No. ANL-78-88, Argonne National Laboratory, 1978.
[54] C.G. Windsor, Pulsed Neutron Scattering, Taylor and Francis, London, 1981.
[55] E.B. Iverson, P.D. Ferguson, F.X. Gallmeier, I.I. Popova, Trans. Am. Nucl. Soc. 89 (2003) 673.
[56] K. Lefman, K. Nielsen, Neutron News 10 (1999) 20.
[57] P. Willendrup, E. Farhi, K. Lefmann, Physica B 250 (2004) 735.
[58] T. Maimaitiyili, A. Steuwer, J. Blomqvist, C.B. C, M.S. Blackmur, O. Zanellato, J. Andrieux, F. Ribeiro, Cryst. Res. Technol. 51 (2016) 663–670.
[59] K. Niedzwiedz, B. Nowak, O.J. Zogal, J. Alloy. Comp. 194 (1993) 47–51.
[60] D. Colognesi, A.J. Ramirez-Cuesta, M. Zoppi, R. Senesi, T. Abdul-Redah, Physica B 350 (2004) e983–e986.
[61] G. Auffermann, G.D. Barrera, D. Colognesi, G. Corradi, A.J. Ramirez-Cuesta, M. Zoppi, J. Phys. Condens. Matter 16 (2004) 5731–5743.

Please cite this article as: T.R. Prisk et al., Vibrational modes and quantum zero-point energy of hydrogen in $ZrH_{0.0155}$ and ZrH_2, Journal of Alloys and Compounds, https://doi.org/10.1016/j.jallcom.2019.152832